

# 3D SHAPE ANALYSIS USING OVERCOMPLETE SPHERICAL WAVELETS: APPLICATION TO BLEB DETECTION IN CELL BIOLOGY

*Robin Tournemenne, Christel Ducroz, Jean-Christophe Olivo-Marin, Alexandre Dufour\**

Institut Pasteur, Quantitative Image Analysis Unit, F-75015 Paris, France  
CNRS URA 2582, Cellular Interactions and Dynamics, F-75015 Paris, France

## ABSTRACT

Amoeboid cell motility is characterised by the emission of protrusions at the cellular surface known as “blebs” [3]. Detection and counting of these blebs is a crucial step towards the understanding of the deformation and motility machinery. We propose an automated technique for bleb detection and counting from cells observed in 3D fluorescence microscopy using spherical wavelet analysis. We improve upon our previous work by adopting a stereographic projection algorithm, which greatly simplifies the manipulation of wavelets on the sphere, leading to a straightforward analogy with traditional wavelets on the plane. We illustrate the detection performance on a real data set of protruding cells, where the proposed approach is able to detect all blebs, and discuss the many possibilities offered by the proposed toolbox for cell shape analysis in general.

**Index Terms**— Spherical wavelets, Shape analysis, Cell morphology, Cell deformation, 3D microscopy

## 1. INTRODUCTION

Cell deformation and motility are dynamic cellular processes regulated by a complex machinery, and have direct implication on the numerous key processes in biology, including development, immune responses and invasive processes [1, 2]. Among the different modes of migration adopted by motile cells, amoeboid motion is of particular interest, as it is adopted by some parasites upon infection as well as metastatic cancer cells. Amoeboid motion is characterised by the formation of protrusions at the cell surface (cf. Fig. 1), which in some cases adhere to the substrate and initiate whole cell movement [3]. A method of choice for studying this mechanism lies in fluorescence microscopy, where protruding cells can be observed over prolonged periods of time in 3D with limited invasiveness. In this work, we are interested in extracting these protrusions at the cell surface in a reliable manner, in a wish to better understand the dynamics of amoeboid cells.

3D shape representation and analysis is a topic of active research in the computer vision and signal processing communities, especially since the advent of modern 3D acquisition and modelling techniques. In the case of 3D biomedical and biological imaging, extensive research is conducted toward the acquisition and analysis of closed shapes at all spatial scales, from molecules [4] to cells [5, 6] and up to entire organs [7, 8]. With the natural variability of shape conformations within so-called homogeneous populations, conventional shape descriptors (volumetric-based, curvature-based, etc.) often lack either robustness or accuracy. Instead, a mathematical framework of choice for the analysis of such surfaces lies on the sphere, where numerous signal processing techniques have been

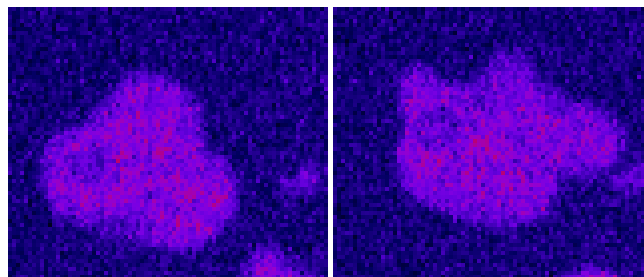


**Fig. 1.** Fluorescence microscopy image of an amoeboid cell undergoing protrusions. Left: before protruding. Right: after protruding. Time between frames: 8 seconds

developed, notably in fields where spherical images are produced [9, 10]. In this context, 2 major representation domains are typically used: spherical harmonics and spherical wavelets. For spherical harmonics (hereafter SPHARM), the signal of interest is projected onto a basis of functions with global support (in analogy with Fourier analysis), and are well suited for global conformation analysis [6]. However, in order to perform local surface analysis and extract features such as cell protrusions, spherical wavelets are particularly well suited, as they provide a function basis with local support.

Spherical wavelets generally come in two flavours, depending on the way they are constructed. The first set of approaches relies on a non-parametric, graph-oriented framework where wavelets are constructed from any arbitrary mesh (not necessarily spherical) via multi-scale decomposition and appropriate lifting schemes [9, 11, 12]. The alternative family of approaches relies on a group-theoretic formulation of wavelet analysis, and extends the framework of over-complete wavelets to the 2-sphere, by transposing into the spherical domain the traditional operations used with wavelets on the plane [13, 14]. Due to its strong analogy with classical wavelets, the framework is well suited for the design of filters with custom properties, such as steerability [15] and self-invertibility [16]. It was also recently shown to provide a more accurate and compact set of descriptors than traditional spherical harmonics in the context of biological shapes [17]. Yet, to the best of our knowledge, feature detection in biology remains to be achieved.

In this work we formulate our shape analysis problem using over-complete wavelets on the sphere, and argue using experimental data that this framework is more robust to heterogeneous surface data than the non-parametric version [18]. The remainder of the paper is organised as follows: section 2 describes the mathematical background of over-complete spherical wavelets; section 3 describes its application to biological shape analysis; section 4 illustrates the method with experimental results; section 5 concludes this work.

\*This work is funded by Institut Pasteur.

## 2. OVER-COMPLETE WAVELETS ON THE SPHERE

**Definition** Let  $x(\theta, \varphi) \in L^2(S^2)$  be a parameterisation of an initial closed surface, with  $\theta \in [0, \pi]$  and  $\varphi \in [0, 2\pi]$ . Traditionally, the calculation of wavelet coefficients  $y$  is given by the inner product between the signal  $x$  and corresponding wavelets with respect to the scale  $n$  and a translation factor. On the sphere, the translation is replaced by a rotation over the 3 Euler angles by  $\alpha, \beta$  and  $\gamma$ , where  $\alpha \in [0, 2\pi]$  defines a rotation about the Z-axis,  $\beta \in [0, \pi]$  defines a rotation about the Y-axis and  $\gamma \in [0, 2\pi]$  defines a final rotation about the Z-axis. Given this notation, the spherical convolution of a signal  $x$  by a filter  $\tilde{h}$  can be written:

$$y_n(\gamma, \beta, \alpha) = \int_{S_2} \tilde{h}_{n,\gamma,\beta,\alpha}^*(\theta, \varphi) x(\theta, \varphi) d\Omega \quad (1)$$

where  $\tilde{h}_{n,\gamma,\beta,\alpha}$  is the angle-dependent analysis filter at scale  $n$ ,  $*$  is the complex conjugation, and  $d\Omega = \sin \theta d\theta d\varphi$ . Unfortunately,  $\tilde{h}$  is dependent of the rotation angle, and computing a filter for each rotation on the sphere is computationally intractable. A solution resides in the SPHARM domain, where a direct connection can be established between the SPHARM coefficients of  $\tilde{h}$  and any of its rotated versions:

$$\tilde{h}_{n,\gamma,\beta,\alpha}^{l,m} = \mathcal{D}_{\gamma,\beta,\alpha}^{l,m}(\tilde{h}_n), \quad \text{with} \quad (2)$$

$$\mathcal{D}_{\gamma,\beta,\alpha}^{l,m}(\tilde{h}_n) = \sum_{m'=-l}^l D_{mm'}^l(\gamma, \beta, \alpha) \tilde{h}_n^{l,m'} \quad (3)$$

where  $l$  and  $m$  are the degree and order of the SPHARM decomposition respectively, and  $D_{mm'}^l$  are the elements of the so-called *Wigner D* matrix, representing the irreducible unitary representations of weight  $l$  of all rotations in  $SO(3)$ . It then comes that the filter value for any angle  $(\theta, \varphi)$  can be obtained via the inverse SPHARM transform:

$$\tilde{h}_{n,\gamma,\beta,\alpha}(\theta, \varphi) = \mathcal{D}_{\gamma,\beta,\alpha}(\tilde{h}_n), \quad \text{with} \quad (4)$$

$$\mathcal{D}_{\gamma,\beta,\alpha}(\tilde{h}_n) = \sum_{l=0}^{\infty} \sum_{m=-l}^l \mathcal{D}_{\gamma,\beta,\alpha}^{l,m}(\tilde{h}_n) \cdot Y^{l,m}(\theta, \varphi) \quad (5)$$

These results imply that an unrotated filter bank  $\{\tilde{h}_n, h_n\}$  is sufficient to fully define the spherical wavelet transform. Going back to eq. (1), wavelet coefficients are now obtained as follows:

$$y_n(\gamma, \beta, \alpha) = \int_{S_2} [\mathcal{D}_{\gamma,\beta,\alpha}(\tilde{h}_n)]^*(\theta, \varphi) x(\theta, \varphi) d\Omega, \quad (6)$$

while synthesis is given by:

$$\hat{x}(\theta, \varphi) = \sum_n \int_{SO(3)} [\mathcal{D}_{\gamma,\beta,\alpha}(h_n)](\theta, \varphi) y_n(\alpha, \beta, \gamma) d\rho \quad (7)$$

where  $d\rho = \sin \beta d\alpha d\beta d\gamma$ .

**Axisymmetric simplification** The present framework stands for any wavelet filter bank. In the specific case of axisymmetric filters however (as will be the case here), further simplifications are introduced. Indeed, such filters are invariant by rotation about the Z-axis by definition, implying that wavelets are now independent of  $\gamma$ , and that  $\forall m \neq 0, h^{l,m} = 0$ . A small development in the SPHARM domain (not shown here due to space limitations) leads to:

$$y(\beta, \alpha)^{l,m} = \sqrt{\frac{4\pi}{2l+1}} x^{l,m} \tilde{h}^{l,0*} \quad (8)$$

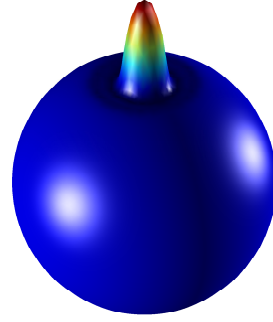


**Fig. 3.** A Laplacian of Gaussian (LoG) filter with  $\sigma = 1$ , mapped on the sphere by inverse stereographic projection.

which drastically simplifies the computation of the wavelet coefficients.

**Stereographic projection and dilation** The last component of the framework is the construction and dilation of wavelets on the sphere. In the group-theoretic paradigm, over-complete wavelets on sphere are built using inverse stereographic projection of wavelets on the plane [13], according to the following formula:

$$\phi_{S^2}(\theta, \varphi) = \left(1 + \tan^2 \frac{\theta}{2}\right) \phi_{\mathbb{R}^2} \left(2 \tan \frac{\theta}{2}, \varphi\right) \quad (9)$$

Thanks to this direct connection between the plane and the sphere, dilation can be carried out in Euclidean space first, and then projected onto the sphere. Analytically, this gives:

$$\phi_{S^2}(\theta, \varphi) = \left(\frac{1 + \tan^2 \frac{\theta}{2}}{1 + (\frac{1}{d} \tan \frac{\theta}{2})^2}\right) \cdot \frac{1}{d} \phi_{\mathbb{R}^2} \left(2 \tan^{-1} \left(\frac{1}{d} \tan \frac{\theta}{2}\right), \varphi\right) \quad (10)$$

where  $d$  is the dilation factor.

## 3. APPLICATION TO BIOLOGICAL SHAPE ANALYSIS

The analysis procedure for each cell surface is depicted in Fig. 2. We describe below the choice of filter for the analysis as well as how we threshold the final coefficients and extract the cell protrusions.

### 3.1. Choice of the wavelet filter

We conducted the wavelet analysis using the Laplacian of Gaussian (LoG) filter, motivated by its popularity in other applications in biology for feature detection. The filter is characterised by a unique parameter  $\sigma$  corresponding to the standard deviation of the underlying Gaussian filter (and is illustrated on the sphere in Fig. 3):

$$LoG(x) = -\frac{1}{\pi\sigma^4} \left[1 - \frac{x^2}{2\sigma^2}\right] e^{-x^2/2\sigma^2} \quad (11)$$

### 3.2. Wavelet coefficient thresholding

Once the wavelet coefficients are computed, we perform an automated threshold based on the universal approach of Donoho and Johnstone [19], defined as follows:

$$\lambda = \frac{MAD(y_n)}{0.6745} \sqrt{2 \log(p)} \quad (12)$$

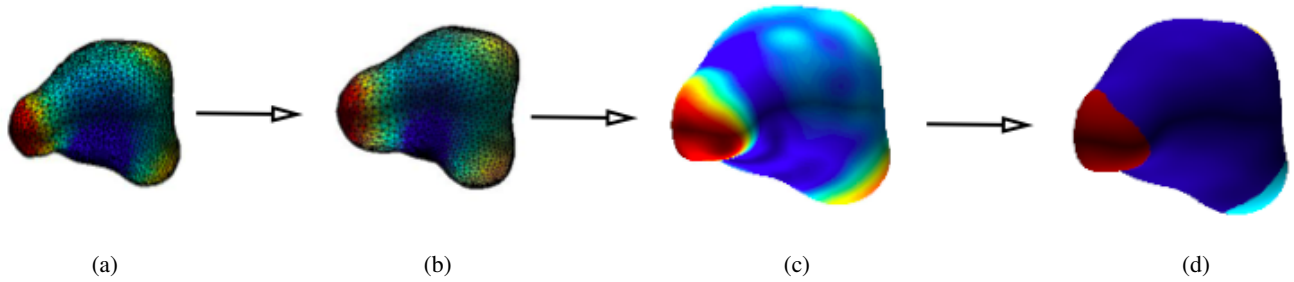


**Fig. 2.** Overview of the analysis workflow. (a) Original cell surface. (b) Parameterised surface. (c) Wavelet coefficients superimposed on the reconstructed surface. (d) Segmentation results. (a) and (b) are coloured with the same spherical signal (obtained after parameterisation) to better visualise the distortions induced by the parameterisation process.

where  $p$  is the total number of Wavelet coefficients at scale  $n$ . It is important to stress that this threshold is based on an asymptotic assumption, and therefore requires a large number of samples. To follow this assumption, we increase the resolution of our extracted mesh surface by resampling the parameterised signal using its SPHARM decomposition.

Once thresholded, a connected component algorithm is applied on the final segmented mesh in order to reconstruct the areas of interest.

## 4. EXPERIMENTAL RESULTS

### 4.1. Data acquisition and surface extraction

The model of study here is the uni-cellular parasite *Entamoeba histolytica*, responsible for the amoebiasis disease. Prior to imaging, parasites are stained with a fluorescent dye and placed in a 3D collagen matrix for 30 minutes. The sample is then observed every 8 seconds for about 12 to 15 minutes under a Nipkow disk confocal microscope equipped with a  $25\times$  objective, yielding time-lapse sequences with 90 to 120 time-points, each of 30 microns thick. The total data set comprises 173 cells, from which we have manually selected 26 cells that summarise the phenotypes observed across the entire population.

After acquisition, cells are segmented and tracked automatically using our 3D active meshes algorithm [20], which generates a triangular mesh surface with homogeneous spatial resolution for each cell tracked.

### 4.2. Detection results on real signals

Fig. 4 present detection results on static cells, while Figs. 5 and 6 present results on time-lapse sequences. These results are highly encouraging: in each case, every extracted area corresponds to a protruding area, and the size of each area matches quite accurately the actual area representing the protrusion. Note that although we are working with an isotropic filter, elongated protrusions are still detected using the universal threshold (Fig. 4-right and Fig. 5). Results on time-lapse sequences of protruding cells (Figs. 5 and 6) additionally indicate that robust tracking of protrusions can be conducted, allowing to measure the dynamics of cell deformation. The observed errors are either due to small protrusions that have not been detected in the selected scale, or due to artefacts induced by the parameterisation process (cf. Fig. 2-(b)).

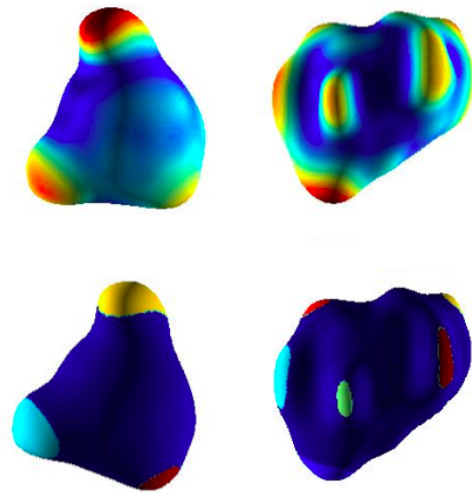


**Fig. 4.** Protrusion detection results on real cells. Top row: wavelet coefficients superimposed on the original surface, colour-coded from blue (low) to red (high). Bottom row: detected protrusions, pseudo-coloured (dark blue indicates no detection).

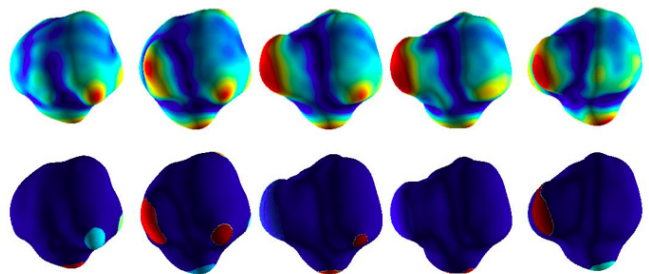


**Fig. 5.** Detection results on a time-lapse sequence. Top row: wavelet coefficients superimposed on the original surface, colour-coded from blue (low) to red (high). Bottom row: detected protrusions, pseudo-coloured (dark blue indicates no detection).

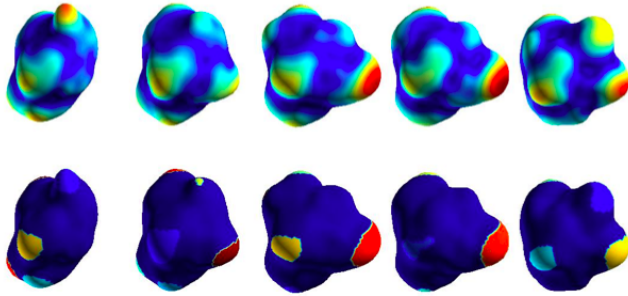


**Fig. 6.** Detection results on a time-lapse sequence. Top row: wavelet coefficients superimposed on the original surface, colour-coded from blue (low) to red (high). Bottom row: detected protrusions, pseudo-coloured (dark blue indicates no detection).

### 4.3. Influence of the parameters and analysis scale

Current results have been obtained using  $\sigma = 1$  for the LoG filter, and only a single scale was used for the thresholding and surface reconstruction (here scale 3). As expected, all protrusions which are clearly visible have been detected by our method, while smaller protrusions have been found in some cases and not others. From a biological point of view, it is in fact visually challenging to assess whether the smaller structures actually correspond to cell protrusions and whether they should be detected or not.

Globally, these results perform more reliably than our previous, non-parametric wavelet approach [18]. This is mostly due to the fact that in the non-parametric approach, the number of coefficients is highly limited by the subdivision level of interest, whereas in the present case each scale of analysis is defined by a large number of coefficients. This stability now permits us to dig in more details into the influence of the size of the filter, and more importantly in investigating multi-scale threshold approaches to detect smaller protrusions that may not be detected accurately in the current setting.

## 5. CONCLUSIONS AND PERSPECTIVES

### 6. REFERENCES

- [1] R. McBeath, D.M. Pirone, C.M. Nelson, K. Bhadriraju, & C.S. Chen. Cell shape, cytoskeletal tension, and RhoA regulate stem cell lineage commitment, *Develop. Cell*, 6(4):483-495, 2004.
- [2] R. Ananthakrishnan, & A. Ehrlicher. The forces behind cell movement, *Int. J Biol Sci.*, 3(5):303-317, 2007.
- [3] B. Maugis, J.Brugues, P. Nassoy, N. Guillen, P. Sens & F. Amblard. Dynamic instability of the intracellular pressure drives bleb-based motility, *Journal of Cell Science*, 123:3884-3892, 2010.
- [4] D.W. Ritchie, & G.J.L. Kemp. Fast Computation, Rotation and Comparison of Low Resolution Spherical Harmonic Molecular Surfaces, *J. Comp. Chemistry*, 20(4):383-395, 1999.
- [5] K. Khairy, J. Foo & J. Howard. Shapes of Red Blood Cells: Comparison of 3D Confocal Images with the Bilayer-couple Model, *Cell. and Mol. Bioeng.*, 1:173-181, 2008.
- [6] C. Ducroz, J.-C. Olivo-Marin & A. Dufour. Characterization of cell shape and deformation in 3D using Spherical Harmonics, in *Proceedings of ISBI*, 848-851, 2012.
- [7] X. Zu, Y. Wang, T.F. Chan, P.M. Thonpson & S.T. Yau. Genus zero surface conformal mapping and its application to brain surface mapping, *IEEE Trans. Med. Imag.*, 23(8):949-958, 2004.
- [8] P. Yu, P. E. Grant, Y. Qi, X. Han, F. Ségonne, R. Pienaar, E. Busa, J. Pacheco, N. Makris, R.L. Buckner, P. Golland & B. Fischl. Cortical Surface Shape Analysis Based on Spherical Wavelets, *IEEE Trans. Med. Imag.*, 26(4):582-597, 2007.
- [9] P. Schröder & W.Sweldens, Spherical Wavelets: Efficiently Representing Functions on the sphere, in *Proceedings of SIGGRAPH 95*, 161-172, 1995.
- [10] R.D. van der Hilst, S. Widiyantro & E.R. Engdahl, Evidence for deep mantle circulation from global tomography. *Nature*, 386:578-584, 1997.
- [11] Wim Sweldens. The Lifting Scheme: A construction of second generation wavelets, *SIAM Journal on Mathematical Analysis*, vol. 29, no. 2, 1997, pp. 511-546.
- [12] C. Lessig & E.Fiume. SOHO: Orthogonal and Symmetric Haar Wavelets on The Sphere, *ACM Trans. Graphics*, 27(1), 2008.
- [13] J-P Antoine & P Vanderghenst. Wavelets on the 2-Sphere: a Group-Theoretical Approach. *Appl. Comput. Harmon. Anal.*, 7:262-291, 1999.
- [14] Y. Wiaux, L. Jacques & P. Vanderghenst. Correspondence principle between spherical and Euclidean wavelets. *The Astrophysical Journal*, 632:820-832, 2005.
- [15] Y. Wiaux, L. Jacques, P. Vielva & P Vanderghenst. Fast directional correlation on the sphere with steerable filters, *The Astrophysical Journal*, 652(1):820, 2006.
- [16] T. Yeo, W. Ou & P. Golland, On the construction of invertible filter banks on the 2-sphere. *IEEE Trans. Im. Proc.*, 17(3):283-300, 2008.
- [17] C.J. Du, J.G. Ferguson, P.T. Hawkins, L.R. Stephens & T. Bretschneider, Local Shape Representation in 3D: from Weighted Spherical Harmonics to Spherical Wavelet. *Proceedings of the British Machine Vision Conference*, pp. 122.1-122.12, 2012.
- [18] C. Ducroz, J.-C. Olivo-Marin & A. Dufour, Characterizing 3D cell shape changes using spherical wavelets. in *Proceedings of ICIP*, 2013, in press.
- [19] D.L. Donoho & I.M. Johnstone. Adapting to Unknown Smoothness via Wavelet Shrinkage. *J. Am. Stat. Soc.*, 90(432):1200-1224, 1995.
- [20] A. Dufour, R. Thibeaux, E. Labruyère, N. Guillen & J.-C. Olivo-Marin. 3D Active Meshes: Fast Discrete Deformable Models for Cell Tracking in 3D Time-Lapse Microscopy. *IEEE Trans. Im. Proc.*, 20(7):1925-1937, 2011.